

# X-Dispersionless Maxwell solver for plasma-based particle acceleration

Alexander Pukhov

*Institut fuer Theoretische Physik I, Universitaet Duesseldorf, 40225 Germany*

(Dated: 06/25/19)

A semi-implicit finite difference time domain (FDTD) numerical Maxwell solver is presented for full electromagnetic Particle-in-Cell (PIC) codes for the simulations of plasma-based acceleration. The solver projects the volumetric Yee lattice into planes transverse to a selected axis (the particle acceleration direction) that makes the scheme quasi-one-dimensional. The scheme removes the numerical dispersion of electromagnetic waves running parallel the selected axis. The field locations in the transverse plane are selected so that the scheme is Lorentz-invariant for relativistic transformations along the selected axis. This completely removes the problem of numerical Cerenkov radiation. The field positions build rhombi-in-plane (RIP) patterns. The RIP scheme uses a compact local stencil that makes it perfectly suitable for massively parallel processing via domain decomposition along all three dimensions. No global/local spectral methods are involved.

## I. INTRODUCTION

Plasma-based particle acceleration is a rapidly developing route towards future compact accelerators [1–4]. The reason is that plasma supports fields orders of magnitude higher than conventional accelerators [5, 6]. Thus, particle acceleration can be accomplished on much shorter distances as compared to solid-state accelerating structures. However, plasma is a highly nonlinear medium and requires accurate and computationally efficient numerical modeling to understand and tune the acceleration process. The main workhorse for plasma simulations are Particle-in-Cell codes [7–11]. These provide the most appropriate description of plasma as an ensemble of particles pushed according to the relativistic equations of motion using self-consistent electromagnetic fields which are maintained on a spatial grid [12].

From a numerical point of view, plasma-based acceleration represents a classic multi-scale problem. Here, we have the long scale of acceleration distance that can range from centimeters [13] to several meters [14, 15], and the short scale of plasma wavelength that ranges from a few micrometers to near millimeter scales. In addition, if the plasma wave is created by a laser pulse, there is additionally the laser wavelength scale in the sub-micron range. This natural scale disparity makes the simulations of plasma-based acceleration so computationally demanding.

Presently, two types of PIC codes are used to simulate the plasma-based accelerator structures: (i) universal full electromagnetic PIC codes [7–11], which solve the unabridged set of Maxwell equations and (ii) quasi-static PIC codes [8, 16, 17], which analytically separate the short scale of plasma wavelength and the long propagation distance scale. The quasi-static PIC codes are proven to be both accurate and very computationally efficient when simulating beam-driven plasma-based wake field acceleration (PBWFA). Unfortunately, the quasi-static approximation for the Maxwell equations eliminates any radiation. Thus, the laser pulse driver has to be described in an envelope approximation [18]. Further, the quasi-static codes fail to correctly model sharp plasma boundaries or self-trapping of particles from background plasma.

For this reason, we here consider full electromagnetic (EM) PIC codes which are usually applied for Laser Wake Field Acceleration (LWFA) in plasmas. The full EM PIC correctly describes the laser evolution even in highly nonlinear regimes. The full EM PIC codes are computationally very expensive because they do not separate the different scales.

A significant scale adjustment can be made if one makes a Lorentz transformation of the system into a reference frame moving in the direction of acceleration with a relativistic speed. This leads to the Lorentz contraction of the propagation distance with the relativistic factor  $\gamma = 1/\sqrt{1 - V^2/c^2}$ , where  $V$  is the relative velocity of the reference frame. Simultaneously, the driver - and its wavelength - become longer at nearly the same factor. This so-called “Lorentz-boost” [19] reduces the scale disparity and potentially gives a large computational speed up.

However, in Lorentz-boosted PIC simulations, the background plasma - both electrons and ions - is moving backward at a relativistic velocity. This streaming plasma is a source of free energy that can be easily transformed into high amplitude noise fields. The major numerical mechanism for this parasitic conversion is the Cerenkov resonance [20]. The problem of existing FDTD Maxwell solvers is that they employ the Yee lattice [21]: individual components of the electromagnetic fields are located at staggered positions in space. The resulting numerical scheme includes a Courant stability restriction on the time step which leads to numerical dispersion. This results in electromagnetic waves with phase velocities below the vacuum speed of light. Thus, relativistic particles may stay in resonance with the waves and radiate. This non-physical Cerenkov radiation plagues the Lorentz-boosted PIC simulations [22]. Moreover, even normal PIC simulations in the laboratory frame suffer from the numerical Cerenkov effect [23, 24]. Any high density bunch of relativistic particles - e.g. the accelerated witness bunch - emits Cerenkov radiation as well. This affects both the bunch energy and emittance [25].

In principle, the Yee scheme can be modified - or extended - by using additional neighbouring cells [26] with the goal to tune the numerical dispersion so that the Cerenkov resonance is avoided in the zero order [27, 28]. This reduces the Cerenkov instability, but does not eliminate it. One of the reasons is that the Yee lattice itself is not Lorentz-invariant. The individual field components are located all at different positions staggered in space. In the boosted frame, the fields are Lorentz-transformed and find themselves at the wrong positions. For example, when the boosted frame moves in the  $X$ -direction, the pairs  $E_y, B_z$  and  $E_z, B_y$  transform one into another. Yet, they are located at different positions within the Yee lattice cell.

## II. PSEUDO-SPECTRAL METHODS AND ALIASING

Recently, pseudo-spectral methods originally proposed by Haber et al. [29] and used by O. Buneman in early versions of his TRISTAN code [30, 31] (changed later to the Yee solver) have seen a remarkable revival [10]. The apparent advantage of the spectral methods is that they are dispersionless and provide an “infinite order” of approximation, with Haber even calling the method a “pseudo-spectral analytical time-domain (PSATD)” algorithm [32].

Indeed, we can write the Maxwell equations in the Fourier space as

$$\frac{\partial \hat{\mathbf{F}}}{\partial t} = c\mathbf{k} \times \hat{\mathbf{F}} - 4\pi \hat{\mathbf{J}} \quad (\text{II.1})$$

where  $\hat{\mathbf{J}} = FFT[\mathbf{J}]$  is the Fourier image of the real current while  $\hat{\mathbf{F}} = FFT[\mathbf{F}]$  is the Fourier image of the complex electromagnetic field  $\mathbf{F} = \mathbf{E} + i\mathbf{B}$ . It is straightforward to show that the numerical scheme advancing the fields from the time step  $n$  to  $n + 1$  in the form

$$\hat{\mathbf{F}}_{\mathbf{k}}^{n+1} = C_{\mathbf{k}} \hat{\mathbf{F}}_{\mathbf{k}}^n + \mathbf{S}_{\mathbf{k}} \times \hat{\mathbf{F}}_{\mathbf{k}}^n - 4\pi \tilde{C}_{\mathbf{k}} \hat{\mathbf{J}}_{\mathbf{k}}^{n+1/2} - 4\pi \tilde{\mathbf{S}}_{\mathbf{k}} \times \hat{\mathbf{J}}_{\mathbf{k}}^{n+1/2} \quad (\text{II.2})$$

is *dispersionless* in vacuum and provides second order approximation for the plasma currents. Here,  $C_{\mathbf{k}} = \cos(ck\tau)$ ,  $\tilde{C}_{\mathbf{k}} = \cos(ck\tau/2)$ ,  $\mathbf{S}_{\mathbf{k}} = \mathbf{e}_{\mathbf{k}} \sin(ck\tau)$ ,  $\tilde{\mathbf{S}}_{\mathbf{k}} = \mathbf{e}_{\mathbf{k}} \sin(ck\tau/2)$ ,  $\tau$  is the time step,  $k = |\mathbf{k}|$ ,  $\mathbf{e}_{\mathbf{k}} = \mathbf{k}/k$ .

Unfortunately, Eq. (II.2) only gives acceptable results on an infinite grid. The reason is that Eq. (II.2) is *not* linear, because it describes the non-linear Vlasov-Maxwell system. The major non-linearity source is the dependence of the current  $\mathbf{J}$  on the fields  $\mathbf{F}$ . The Fourier transform, however, is a linear operator. When applied to a non-linear system, it causes aliasing [34]. Moreover, even the terms linear in  $\mathbf{F}$ , but containing products with the wave vector  $\mathbf{k}$  are subject to aliasing. Let us take the seemingly harmless product  $C_{\mathbf{k}} \hat{\mathbf{F}}_{\mathbf{k}}^n$ . In configuration space on a finite grid with  $M$  cells (for simplicity, we take a 1D example), it corresponds to the convolution

$$FFT^{-1} \left[ C_{\mathbf{k}} \hat{\mathbf{F}}_{\mathbf{k}}^n \right]_l = \sum_{m=1}^M FFT^{-1} [C_{\mathbf{k}}]_m \mathbf{F}_{l-m}^n \quad (\text{II.3})$$

For indices in the range  $l - m < 0$ , the convolution (II.3) overruns the finite grid boundary and automatically takes field values  $\mathbf{F}_{M+l-m}^n$  from the opposite end of the grid. This makes little physical sense and is generally called “aliasing” of the pseudo-spectral methods [35]. All other products of two functions depending on  $\mathbf{k}$ , such as  $\mathbf{S}_{\mathbf{k}}$ ,  $\tilde{C}_{\mathbf{k}}$  and  $\tilde{\mathbf{S}}_{\mathbf{k}}$  in (II.2) result in unphysical aliasing as well. This makes the pseudo-spectral schemes unphysical unless some “de-aliasing” procedure removes these effects.

The aliasing of the  $\mathbf{k}$ -products in (II.2) can be removed in a relatively straightforward way: the arrays of images in the configuration space must be “padded” by zeroes so that the aliased convolution does not touch non-zero values from the other side [36]. This de-aliasing procedure works well for equations with *quadratic* nonlinearities even though it may be expensive in multi-dimensional simulations.

The pseudo-spectral PIC codes, however, contain another nonlinearity that is not quadratic at all and is a much more severe source of aliasing. The current  $\mathbf{J}$  has a highly nonlinear dependence on the fields, and thus its Fourier image  $\hat{\mathbf{J}}[\mathbf{F}]$  used in (II.2) is fully aliased. This can be readily seen even in the hydrodynamic version of the current

$$\mathbf{J} = qn\mathbf{p}/m\gamma, \quad (\text{II.4})$$

where  $n(\mathbf{r})$  is the particle density. For example, a low-amplitude harmonic field  $\mathbf{E}(\mathbf{r}, t) = \Re[\mathbf{E}_0(\mathbf{r}) \exp(-i\omega t)]$  leads to a local momentum  $\mathbf{p} = \Re[i\mathbf{E}/q\omega]$ . Transforming (II.4) to the Fourier space, we have

$$\tilde{\mathbf{J}} = \frac{1}{im\omega} FFT[n(\mathbf{r})\mathbf{E}(\mathbf{r})/\gamma(\mathbf{E})] \quad (\text{II.5})$$

For the simplest non-relativistic ( $\gamma = 1$ ) hydrodynamic case, the Fourier image of the product (II.5) corresponds to a convolution in the Fourier space

$$\tilde{\mathbf{J}} = \frac{1}{im\omega} \sum_{k=-K/2}^{K/2-1} \tilde{n}_k \mathbf{E}_{K/2-k} \quad (\text{II.6})$$

where  $K$  is the number of modes. This convolution aliases spectra of the particle density  $\tilde{n}_k$  and the field  $\mathbf{E}_{K/2-k}$ . The simplest non-relativistic hydrodynamic case (II.6) corresponds to the quadratic nonlinearity and could be corrected by padding. However, the physical quantities in full PIC codes cannot be described by this oversimplified approximation. For example, as the field becomes large, the particle velocity depends on the relativistic  $\gamma$ -factor of

particles  $\gamma = \sqrt{1 + \mathbf{p}^2/m^2c^2}$ , which depends on the fields in a highly nonlinear way. Further, the macroparticle shape function has to be used to interpolate the fields and deposit currents on the grid. Thus, the current  $\mathbf{J}$  depends on the fields in a non-quadratic non-local non-linear way. The calculation of  $\mathbf{J}$  does not correspond to a simple convolution in Fourier-space. This leads to a heavy aliasing of the pseudo-spectral currents  $\tilde{\mathbf{J}}$  that cannot be removed in any easy way.

The physical signatures of this aliasing will manifest in different ways depending on the particular physics of the problem, ranging from global artefacts sometimes clearly seen on the grid, to potential non-convergence of pseudo-spectral codes. One of these signatures is the persistence of Cerenkov instability in pseudo-spectral codes despite the absence of numerical dispersion [37]. In this case, it arises due to particles interacting with waves from the upper numerical Brillouin zone. In an effort to remove the Cerenkov instability in pseudo-spectral codes, filtering currents of the most unstable modes is often applied [38]. This artificial filtering, however, may lead to additional unphysical effects in the pseudo-spectral simulations.

We conclude that pseudo-spectral methods are far from ideal candidates for PIC simulations and that a better FDTD method is required. In this work, a new FDTD solver is presented that does not employ spectral transformations and yet has the unique property of having no numerical dispersion along one selected spatial direction. The solver uses Lorentz-invariant field locations for transformations along this selected axis, and so particles moving in this direction do not generate non-physical Cerenkov radiation.

### III. THE GENERAL QUASI-1D MAXWELL SOLVER

We here develop a FDTD 3D Maxwell solver which has no numerical dispersion for plane waves propagating one selected direction. In plasma-based acceleration this is usually the direction of particle acceleration: the driving laser optical axis. The solver should remain free of numerical dispersion regardless of the plasma density, from vacuum up to dense plasmas, i.e. the optimal time step/grid step relation should not be compromised by the presence of plasma. The solver must not use spectral transformations and should have a compact local stencil. This is the pre-requisite for efficient parallelization via domain decomposition. In short, we develop an efficient Maxwell solver for quasi-1D problems.

We select the  $X$ -direction for dispersionless propagation. For electromagnetic waves propagating in  $X$ , we have the Maxwell equations

$$\frac{\partial E_y}{c\partial t} = -\frac{\partial B_z}{\partial x} + \Gamma_y \quad (\text{III.1})$$

$$\frac{\partial E_z}{c\partial t} = \frac{\partial B_y}{\partial x} + \Gamma_z \quad (\text{III.2})$$

$$\frac{\partial E_x}{c\partial t} = \Gamma_x \quad (\text{III.3})$$

$$\frac{\partial B_y}{c\partial t} = \frac{\partial E_z}{\partial x} + \Phi_y \quad (\text{III.4})$$

$$\frac{\partial B_z}{c\partial t} = -\frac{\partial E_y}{\partial x} + \Phi_z \quad (\text{III.5})$$

$$\frac{\partial B_x}{c\partial t} = \Phi_x \quad (\text{III.6})$$

Here, the vector  $\bar{\Gamma} = \mathbf{G} + \mathbf{J}$  combines the vacuum diffraction  $\mathbf{G}$  for  $\mathbf{E}$  and the medium response (currents)  $\mathbf{J}$ , while  $\bar{\Phi}$  is the vacuum diffraction operator for  $\mathbf{B}$ .

We use a semi-implicit trapezoidal scheme for the discretization of the transverse fields on a 3D grid. We write here explicitly the  $i$ -index along the  $X$ -axis only as the scheme can be easily generalized for arbitrary transverse geometries (e.g. Cartesian, or cylindrical, unstructured, etc.):

$$\frac{E_{y(i+1)}^{n+1} + E_{y(i)}^{n+1} - E_{y(i+1)}^n - E_{y(i)}^n}{2c\tau} = -\frac{-B_{z(i)}^{n+1} + B_{z(i+1)}^{n+1} - B_{z(i)}^n + B_{z(i+1)}^n}{2h_x} + \Gamma_{y(i+1/2)}^{n+1/2} \quad (\text{III.7})$$

$$\frac{E_{z(i+1)}^{n+1} + E_{z(i)}^{n+1} - E_{z(i+1)}^n - E_{z(i)}^n}{2c\tau} = \frac{-B_{y(i)}^{n+1} + B_{y(i+1)}^{n+1} - B_{y(i)}^n + B_{y(i+1)}^n}{2h_x} + \Gamma_{z(i+1/2)}^{n+1/2} \quad (\text{III.8})$$

$$\frac{E_{x(i)}^{n+1} - E_{x(i)}^n}{c\tau} = \Gamma_{x(i)}^{n+1/2} \quad (\text{III.9})$$

$$\frac{B_{y(i)}^{n+1} + B_{y(i+1)}^{n+1} - B_{y(i)}^n - B_{y(i+1)}^n}{2c\tau} = \frac{-E_{z(i)}^{n+1} + E_{z(i+1)}^{n+1} - E_{z(i)}^n + E_{z(i+1)}^n}{2h_x} + \Phi_{y(i+1/2)}^{n+1/2} \quad (\text{III.10})$$

$$\frac{B_{z(i)}^{n+1} + B_{z(i+1)}^{n+1} - B_{z(i)}^n - B_{z(i+1)}^n}{2c\tau} = -\frac{-E_{y(i)}^{n+1} + E_{y(i+1)}^{n+1} - E_{y(i)}^n + E_{y(i+1)}^n}{2h_x} + \Phi_{z(i+1/2)}^{n+1/2} \quad (\text{III.11})$$

$$\frac{B_{x(i)}^{n+1} - B_{x(i)}^n}{c\tau} = \Phi_{x(i)}^{n+1/2} \quad (\text{III.12})$$

Here,  $\tau$  is the time step and  $h_x$  is the spatial grid step in the  $X$ -direction.

These equations (III.7)-(III.12) build a system of linear equations relating the updated fields at the time step  $n+1$  with already known fields at the time steps  $n$  and  $n+1/2$ . Although this implicit system of linear equations can generally be solved using a fast matrix inversion method (the system has a sparse matrix), we will be interested in the **special case**  $c\tau = h_x = \Delta$ . In this particular case, the inversion is straightforward.

First, we add Eqs. (III.7)+(III.11) and (III.8)+(III.10) to obtain transport components

$$T_{y(i)}^{+(n+1)} = E_{y(i)}^{n+1} + B_{z(i)}^{n+1} = E_{y(i-1)}^n + B_{z(i-1)}^n + \Delta \left( \Gamma_{y(i-1/2)}^{n+1/2} + \Phi_{z(i-1/2)}^{n+1/2} \right) \quad (\text{III.13})$$

$$T_{z(i)}^{+(n+1)} = E_{z(i)}^{n+1} + B_{y(i)}^{n+1} = E_{z(i+1)}^n + B_{y(i+1)}^n + \Delta \left( \Gamma_{z(i+1/2)}^{n+1/2} + \Phi_{y(i+1/2)}^{n+1/2} \right) \quad (\text{III.14})$$

or simply

$$T_{y(i)}^{+(n+1)} = T_{y(i-1)}^{+(n)} + \Delta \left( \Gamma_{y(i-1/2)}^{n+1/2} + \Phi_{z(i-1/2)}^{n+1/2} \right) \quad (\text{III.15})$$

$$T_{z(i)}^{+(n+1)} = T_{z(i+1)}^{+(n)} + \Delta \left( \Gamma_{z(i+1/2)}^{n+1/2} + \Phi_{y(i+1/2)}^{n+1/2} \right) \quad (\text{III.16})$$

Then, we subtract the same Eqs. (III.7)-(III.11) and (III.8)-(III.10) to obtain

$$T_{y(i)}^{-(n+1)} = E_{y(i)}^{n+1} - B_{z(i)}^{n+1} = E_{y(i+1)}^n - B_{z(i+1)}^n + \Delta \left( \Gamma_{y(i+1/2)}^{n+1/2} - \Phi_{z(i+1/2)}^{n+1/2} \right) \quad (\text{III.17})$$

$$T_{z(i)}^{-(n+1)} = E_{z(i)}^{n+1} - B_{y(i)}^{n+1} = E_{z(i-1)}^n - B_{y(i-1)}^n + \Delta \left( \Gamma_{z(i-1/2)}^{n+1/2} - \Phi_{y(i-1/2)}^{n+1/2} \right) \quad (\text{III.18})$$

or

$$T_{y(i)}^{-(n+1)} = T_{y(i+1)}^{-(n)} + \Delta \left( \Gamma_{y(i+1/2)}^{n+1/2} - \Phi_{z(i+1/2)}^{n+1/2} \right) \quad (\text{III.19})$$

$$T_{z(i)}^{-(n+1)} = T_{z(i-1)}^{-(n)} + \Delta \left( \Gamma_{z(i-1/2)}^{n+1/2} - \Phi_{y(i-1/2)}^{n+1/2} \right) \quad (\text{III.20})$$

These are the marching equations. The transport components  $T_{y,z}^{+/-}$  must be shifted one cell in the corresponding direction and the diffraction/refraction terms be correctly added.

For the fields, we get

$$E_{y(i)}^{n+1} = \frac{1}{2} \left( E_{y(i-1)}^n + E_{y(i+1)}^n \right) - \frac{1}{2} \left( B_{z(i+1)}^n - B_{z(i-1)}^n \right) \quad (\text{III.21})$$

$$\begin{aligned} & + \frac{\Delta}{2} \left( \Gamma_{y(i-1/2)}^{n+1/2} + \Phi_{z(i-1/2)}^{n+1/2} + \Gamma_{y(i+1/2)}^{n+1/2} - \Phi_{z(i+1/2)}^{n+1/2} \right) \\ E_{z(i)}^{n+1} & = \frac{1}{2} \left( E_{z(i-1)}^n + E_{z(i+1)}^n \right) + \frac{1}{2} \left( B_{y(i+1)}^n - B_{y(i-1)}^n \right) \quad (\text{III.22}) \\ & + \frac{\Delta}{2} \left( \Gamma_{z(i-1/2)}^{n+1/2} - \Phi_{y(i-1/2)}^{n+1/2} + \Gamma_{z(i+1/2)}^{n+1/2} + \Phi_{y(i+1/2)}^{n+1/2} \right) \end{aligned}$$

$$B_{y(i)}^{n+1} = \frac{1}{2} \left( B_{y(i-1)}^n + B_{y(i+1)}^n \right) + \frac{1}{2} \left( E_{z(i+1)}^n - E_{z(i-1)}^n \right) \quad (\text{III.23})$$

$$\begin{aligned} & + \frac{\Delta}{2} \left( -\Gamma_{z(i-1/2)}^{n+1/2} + \Phi_{y(i-1/2)}^{n+1/2} + \Gamma_{z(i+1/2)}^{n+1/2} + \Phi_{y(i+1/2)}^{n+1/2} \right) \\ B_{z(i)}^{n+1} & = \frac{1}{2} \left( B_{z(i-1)}^n + B_{z(i+1)}^n \right) - \frac{1}{2} \left( E_{y(i+1)}^n - E_{y(i-1)}^n \right) \quad (\text{III.24}) \\ & + \frac{\Delta}{2} \left( \Gamma_{y(i-1/2)}^{n+1/2} + \Phi_{z(i-1/2)}^{n+1/2} - \Gamma_{y(i+1/2)}^{n+1/2} + \Phi_{z(i+1/2)}^{n+1/2} \right) \end{aligned}$$

or simply

$$E_{y(i)}^{(n+1)} = \frac{T_{y(i)}^{+(n+1)} + T_{y(i)}^{-(n+1)}}{2} \quad (\text{III.25})$$

$$E_{z(i)}^{(n+1)} = \frac{T_{z(i)}^{+(n+1)} + T_{z(i)}^{-(n+1)}}{2} \quad (\text{III.26})$$

$$B_{y(i)}^{(n+1)} = \frac{T_{y(i)}^{+(n+1)} - T_{y(i)}^{-(n+1)}}{2} \quad (\text{III.27})$$

$$B_{z(i)}^{(n+1)} = \frac{T_{z(i)}^{+(n+1)} - T_{z(i)}^{-(n+1)}}{2} \quad (\text{III.28})$$

#### IV. THE THREE-DIMENSIONAL RIP MAXWELL SOLVER IN CARTESIAN COORDINATES

Let us now look at the diffraction/refraction terms. For simplicity, we use Cartesian coordinates.

We project the Yee lattice onto the  $(Y, Z)$  plane. The grid becomes planar and has the form of Rhombi-in-Plane (RIP), as shown in Fig. 1. The pairs of transverse fields are now combined at positions according to the transport properties (III.13)-(III.14). The pair  $\mathbf{E}_y, \mathbf{B}_z$  is located at the grid vertices  $(i, j + 1/2, k)$ . The pair  $\mathbf{E}_z, \mathbf{B}_y$  is located at the grid vertices  $(i, j, k + 1/2)$ . The longitudinal field  $\mathbf{E}_x$  we place at point  $(i, j, k)$  which is the center of the full integer rhombus. The longitudinal field  $\mathbf{B}_x$  we place at the center of the half integer rhombus  $(i, j + 1/2, k + 1/2)$ . The grid is shown in Fig.IV.1.

Then, the diffraction/refraction terms at the half time step will be:

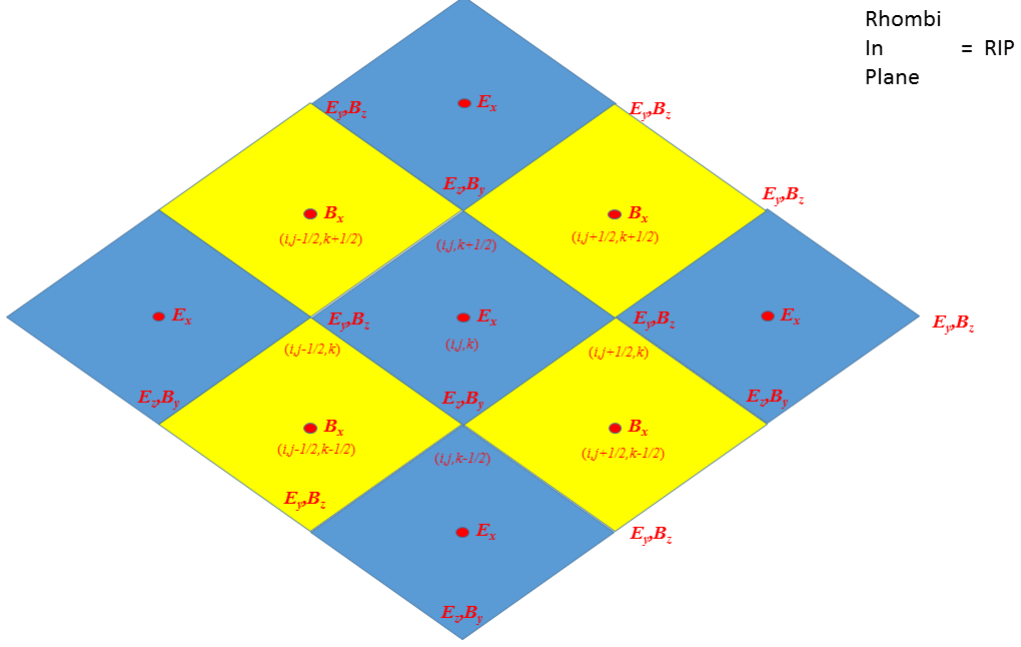


Figure IV.1. The “rhombi-in-plane” RIP grid. Blue rhombi are centered at integer nodes  $(i, j, k)$ . The yellow rhombi have centers staggered by half grid steps in the transverse plane  $(i, j + 1/2, j + 1/2)$ .

$$\Gamma_{y(i+1/2, j+1/2, k)}^{n+1/2} = \left( \frac{\partial B_x}{\partial z} - \frac{4\pi}{c} j_y \right) \Big|_{i+1/2, j+1/2, k}^{n+1/2} = -\frac{2\pi}{c} \left( j_{y, (i, j+1/2, k)}^{n+1/2} + j_{y, (i+1, j+1/2, k)}^{n+1/2} \right) + \quad (IV.1)$$

$$+ \frac{B_{x(i, j+1/2, k+1/2)}^{n+1/2} + B_{x(i+1, j+1/2, k+1/2)}^{n+1/2} - B_{x(i, j+1/2, k-1/2)}^{n+1/2} - B_{x(i+1, j+1/2, k-1/2)}^{n+1/2}}{2h_z}$$

$$\Gamma_{z(i+1/2, j, k+1/2)}^{n+1/2} = \left( -\frac{\partial B_x}{\partial y} - \frac{4\pi}{c} j_y \right) \Big|_{i+1/2, j, k+1/2}^{n+1/2} = -\frac{2\pi}{c} \left( j_{z, (i, j, k+1/2)}^{n+1/2} + j_{z, (i+1, j, k+1/2)}^{n+1/2} \right) - \quad (IV.2)$$

$$- \frac{B_{x(i, j+1/2, k+1/2)}^{n+1/2} + B_{x(i+1, j+1/2, k+1/2)}^{n+1/2} - B_{x(i, j-1/2, k+1/2)}^{n+1/2} - B_{x(i+1, j-1/2, k+1/2)}^{n+1/2}}{2h_y}$$

$$\Gamma_{x(i, j, k)}^{n+1/2} = \left( \frac{\partial B_z}{\partial y} - \frac{\partial B_y}{\partial z} + \frac{4\pi}{c} j_x \right) \Big|_{i, j, k}^{n+1/2} = -\frac{4\pi}{c} j_{x, (i, j, k)}^{n+1/2} \quad (IV.3)$$

$$+ \frac{B_{z(i, j+1/2, k)}^{n+1/2} - B_{z(i, j-1/2, k)}^{n+1/2}}{h_y} - \frac{B_{y(i, j, k+1/2)}^{n+1/2} - B_{y(i, j, k-1/2)}^{n+1/2}}{h_z}$$

$$\Phi_{y(i+1/2, j, k+1/2)}^{n+1/2} = -\frac{E_{x(i, j, k+1)}^{n+1/2} + E_{x(i+1, j, k+1)}^{n+1/2} - E_{x(i, j, k)}^{n+1/2} - E_{x(i+1, j, k)}^{n+1/2}}{2h_z} \quad (IV.4)$$

$$\Phi_{z(i+1/2, j+1/2, k)}^{n+1/2} = \frac{E_{x(i, j+1, k)}^{n+1/2} + E_{x(i+1, j+1, k)}^{n+1/2} - E_{x(i, j, k)}^{n+1/2} - E_{x(i+1, j, k)}^{n+1/2}}{2h_y} \quad (IV.5)$$

$$\Phi_{x(i, j+1/2, k+1/2)}^{n+1/2} = -\left( \frac{\partial E_z}{\partial y} - \frac{\partial E_y}{\partial z} \right) \Big|_{i, j+1/2, k+1/2}^{n+1/2} = \quad (IV.6)$$

$$- \frac{E_{z(i, j+1, k+1/2)}^{n+1/2} - E_{z(i, j, k+1/2)}^{n+1/2}}{h_y} + \frac{E_{y(i, j+1/2, k+1)}^{n+1/2} - E_{y(i, j-1/2, k+1/2)}^{n+1/2}}{h_z}$$

Similar formulas are obtained for the fields at the half-time steps. After straightforward manipulations, we get the simple marching equations

$$T_{y(i+1/2)}^{+(n+1/2)} = T_{y(i-1/2)}^{+(n-1/2)} + \Delta \left( G_{y(i)}^n + F_{z(i)}^n \right) \quad (\text{IV.7})$$

$$T_{z(i-1/2)}^{+(n+1/2)} = T_{z(i+1/2)}^{+(n-1/2)} + \Delta \left( G_{z(i)}^n + F_{y(i)}^n \right) \quad (\text{IV.8})$$

$$T_{y(i-1/2)}^{-(n+1/2)} = T_{y(i+1/2)}^{-(n-1/2)} + \Delta \left( G_{y(i)}^{n+1/2} - F_{z(i)}^{n+1/2} \right) \quad (\text{IV.9})$$

$$T_{z(i+1/2)}^{-(n+1/2)} = T_{z(i-1/2)}^{-(n-1/2)} + \Delta \left( G_{z(i)}^{n+1/2} - F_{y(i)}^{n+1/2} \right) \quad (\text{IV.10})$$

with the diffraction/refraction terms

$$\begin{aligned} \Gamma_{y(i+1/2,j+1/2,k)}^n &= \left( \frac{\partial B_x}{\partial z} - \frac{4\pi}{c} j_y \right)_{i+1/2,j+1/2,k}^n = -\frac{2\pi}{c} \left( j_{y,(i,j+1/2,k)}^n + j_{y,(i+1,j+1/2,k)}^n \right) + \\ &+ \frac{B_{x(i,j+1/2,k+1/2)}^{n+1/2} + B_{x(i+1,j+1/2,k+1/2)}^{n+1/2} - B_{x(i,j+1/2,k-1/2)}^{n+1/2} - B_{x(i+1,j+1/2,k-1/2)}^{n+1/2}}{2h_z} \end{aligned} \quad (\text{IV.11})$$

$$\begin{aligned} \Gamma_{z(i+1/2,j,k+1/2)}^n &= \left( -\frac{\partial B_x}{\partial y} - \frac{4\pi}{c} j_y \right)_{i+1/2,j,k+1/2}^n = -\frac{2\pi}{c} \left( j_{z,(i,j,k+1/2)}^n + j_{z,(i+1,j,k+1/2)}^n \right) - \\ &- \frac{B_{x(i,j+1/2,k+1/2)}^n + B_{x(i+1,j+1/2,k+1/2)}^n - B_{x(i,j-1/2,k+1/2)}^n - B_{x(i+1,j-1/2,k+1/2)}^n}{2h_y} \end{aligned} \quad (\text{IV.12})$$

$$\begin{aligned} \Gamma_{x(i,j,k)}^n &= \left( \frac{\partial B_z}{\partial y} - \frac{\partial B_y}{\partial z} + \frac{4\pi}{c} j_x \right)_{i,j,k}^n = -\frac{4\pi}{c} j_{x,(i,j,k)}^n \\ &+ \frac{B_{z(i,j+1/2,k)}^n - B_{z(i,j-1/2,k)}^n}{h_y} - \frac{B_{y(i,j,k+1/2)}^n - B_{y(i,j,k-1/2)}^n}{h_z} \end{aligned} \quad (\text{IV.13})$$

$$\Phi_{y(i+1/2,j,k+1/2)}^n = -\frac{E_{x(i,j,k+1)}^n + E_{x(i+1,j,k+1)}^n - E_{x(i,j,k)}^n - E_{x(i+1,j,k)}^n}{2h_z} \quad (\text{IV.14})$$

$$\Phi_{z(i+1/2,j+1/2,k)}^n = \frac{E_{x(i,j+1,k)}^n + E_{x(i+1,j+1,k)}^n - E_{x(i,j,k)}^n - E_{x(i+1,j,k)}^n}{2h_y} \quad (\text{IV.15})$$

$$\begin{aligned} \Phi_{x(i,j+1/2,k+1/2)}^n &= -\left( \frac{\partial E_z}{\partial y} - \frac{\partial E_y}{\partial z} \right)_{i,j+1/2,k+1/2}^n = \\ &- \frac{E_{z(i,j+1,k+1/2)}^n - E_{z(i,j,k+1/2)}^n}{h_y} + \frac{E_{y(i,j+1/2,k+1)}^n - E_{y(i,j-1/2,k+1/2)}^n}{h_z} \end{aligned} \quad (\text{IV.16})$$

The use of the transport vectors  $\mathbf{T}_\perp$  makes the boundary conditions in the  $X$ -direction trivial.

It seems that we have to maintain two sets of fields for each time step: fields at the full step and at the half step. The particles however, can be pushed just once per time step using the Lorentz-invariant [19] trapezoidal semi-implicit scheme at the full step:

$$\mathbf{p}_\alpha^{n+1/2} = \mathbf{p}_\alpha^{n-1/2} + \tau q \left( \mathbf{E}^n + \frac{\mathbf{v}_\alpha^{n+1/2} + \mathbf{v}_\alpha^{n-1/2}}{2c} \mathbf{B}^n \right) \quad (\text{IV.17})$$

where  $\mathbf{v}_\alpha = \mathbf{p}_\alpha / \gamma_\alpha mc$  is velocity of the macroparticle  $\alpha$ . This particle push generates currents  $\mathbf{j}^{n+1/2}$  at the half time steps. Currents at the full time step required to push the half-time step fields can be obtained by simple averaging on the grid

$$\mathbf{j}^n = \frac{1}{2} \left( \mathbf{j}^{n-1/2} + \mathbf{j}^{n+1/2} \right) \quad (\text{IV.18})$$



To ensure the Lorentz invariance of the scheme, the current components are defined within the cell at the same positions as the corresponding  $\mathbf{E}$ -field components.

The RIP scheme places fields in a transverse plane as seen in Fig.IV.1. These field locations prevent a strictly conservative definition of the currents and the fields on the grid. Thus, the numerical continuity equation is not rigorously satisfied. However, using high order interpolation schemes for the current deposition and following particle trajectories inside the cells [39], one can fulfill the continuity equation with high accuracy.

The fields at the half-time steps are required to calculate the diffraction terms only. Without diffraction, the need to maintain the additional set of fields at half-time steps vanishes and the RIP scheme becomes identical to the standard 1D PIC scheme [12], which is the workhorse of 1D plasma PIC simulations.

## V. DISPERSION AND STABILITY OF THE RIP SCHEME

We apply the plane-wave analysis to the marching equations (III.9), (III.12) and (III.21)-(III.24) with the refraction/diffraction terms (IV.1)-(IV.6) assuming  $\mathbf{F} = \tilde{\mathbf{F}} \exp(-i\omega t + i\mathbf{k}\mathbf{r})$ . For simplicity, we assume uniform plasma frequency  $\omega_p^2 = 4\pi n e^2 / \gamma$  and a linear current response to the electric field  $4\pi \frac{2c}{\Delta} \sin \frac{\omega\tau}{2} \tilde{\mathbf{J}} = i\omega_p^2 \tilde{\mathbf{E}}$ . For the case of interest,  $c\tau = h_x = \Delta$ , these equations become

$$\frac{2}{\Delta} \sin \frac{\omega\Delta}{2c} \cos \frac{k_x\Delta}{2} \tilde{E}_y = -\frac{2}{\Delta} \sin \frac{k_x\Delta}{2} \cos \frac{\omega\Delta}{2c} \tilde{B}_z \quad (\text{V.1})$$

$$+ \frac{2}{h_z} \sin \frac{k_z h_z}{2} \cos \frac{k_x\Delta}{2} \tilde{B}_x + \omega_p^2 \frac{\Delta}{2c \sin \frac{\omega\Delta}{2c}} \tilde{E}_y$$

$$\frac{2}{\Delta} \sin \frac{\omega\Delta}{2c} \cos \frac{k_x\Delta}{2} \tilde{E}_z = \frac{2}{\Delta} \sin \frac{k_x\Delta}{2} \cos \frac{\omega\Delta}{2c} \tilde{B}_y \quad (\text{V.2})$$

$$- \frac{2}{h_y} \sin \frac{k_y h_y}{2} \cos \frac{k_x\Delta}{2} \tilde{B}_x + \omega_p^2 \frac{\tau}{2 \sin \frac{\omega\tau}{2}} \tilde{E}_z$$

$$\frac{2}{\Delta} \sin \frac{\omega\Delta}{2c} \tilde{E}_x = \frac{2}{h_y} \sin \frac{k_y h_y}{2} \tilde{B}_z - \frac{2}{h_z} \sin \frac{k_z h_z}{2} \tilde{B}_y \quad (\text{V.3})$$

$$+ \omega_p^2 \frac{\Delta}{2c \sin \frac{\omega\Delta}{2c}} \tilde{E}_x \quad (\text{V.4})$$

$$\frac{2}{\Delta} \sin \frac{\omega\Delta}{2c} \cos \frac{k_x\Delta}{2} \tilde{B}_y = \frac{2}{\Delta} \sin \frac{k_x\Delta}{2} \cos \frac{\omega\Delta}{2c} \tilde{E}_z \quad (\text{V.5})$$

$$- \frac{2}{h_z} \sin \frac{k_z h_z}{2} \cos \frac{k_x h_x}{2} \tilde{E}_x$$

$$\frac{2}{\Delta} \sin \frac{\omega\Delta}{2c} \cos \frac{k_x\Delta}{2} \tilde{B}_z = -\frac{2}{\Delta} \sin \frac{k_x\Delta}{2} \cos \frac{\omega\Delta}{2c} \tilde{E}_y \quad (\text{V.6})$$

$$+ \frac{2}{h_y} \sin \frac{k_y h_y}{2} \cos \frac{k_x h_x}{2} \tilde{E}_x$$

$$\frac{2}{\Delta} \sin \frac{\omega\tau}{2} \tilde{B}_x = \frac{2}{k_y h_y} \sin \frac{k_y h_y}{2} \tilde{E}_z - \frac{2}{k_z h_z} \sin \frac{k_z h_z}{2} \tilde{E}_y \quad (\text{V.7})$$

The dispersion relation in vacuum ( $\omega_p = 0$ ) is rather simple:

$$\left( \frac{1}{h_y^2} \sin^2 \frac{k_y h_y}{2} + \frac{1}{h_z^2} \sin^2 \frac{k_z h_z}{2} \right) + \frac{1}{\Delta^2} \sin^2 \frac{\Delta k_x}{2} \left( 1 - \Delta^2 \left( \frac{1}{h_y^2} \sin^2 \frac{k_y h_y}{2} + \frac{1}{h_z^2} \sin^2 \frac{k_z h_z}{2} \right) \right) = \frac{1}{\Delta^2} \sin^2 \frac{\Delta\omega}{2c} \quad (\text{V.8})$$

The stability condition in vacuum is

$$\Delta^2 \left( \frac{1}{h_y^2} + \frac{1}{h_z^2} \right) < 1 \quad (\text{V.9})$$

In the presence of plasmas, it is modified to

$$\frac{1}{\Delta^2} > \frac{1}{h_y^2} + \frac{1}{h_z^2} + \frac{c^2 \omega_p^2}{4} \quad (\text{V.10})$$

The RIP scheme combines dispersionless properties of the standard 1D solver along the  $X$ -axis with the Yee dispersion for waves running in the transverse direction. Indeed, setting  $k_y = k_z = 0$  in the dispersion relation (V.8), we immediately obtain  $\omega = ck_x$  and the phase velocity

$$V_{ph} = \frac{\omega}{k_x} = c \quad (\text{V.11})$$

for plane waves propagating in the  $X$ -direction.

Conversely, setting  $k_x = 0$ , we obtain the usual 2D Yee dispersion relation for waves propagating in the transverse direction

$$\frac{1}{h_y^2} \sin^2 \frac{k_y h_y}{2} + \frac{1}{h_z^2} \sin^2 \frac{k_z h_z}{2} = \frac{1}{\Delta^2} \sin^2 \frac{\Delta \omega}{2c} \quad (\text{V.12})$$

with all its known advantages and drawbacks.

## VI. NUMERICAL TESTS OF THE RIP MAXWEL SOLVER

### A. Cerenkov instability test

As a first test, we take the numerical Cerenkov instability. We compare the standard Yee solver and the RIP solver, both implemented on the VLPL platform [8]. No artificial filtering of fields or currents is used. The initial configuration is a spherical plasma with a Gaussian density profile  $n = n_0 \exp(-r^2/\sigma^2)$  consisting of electrons and protons moving in the  $X$ -direction with the average momentum  $\langle \mathbf{p}_0 \rangle / m_\alpha c = (p_{x0}, 0, 0)$ , where  $\alpha$  denotes the particle type ( $\alpha = e, p$ ), with  $m_p/m_e = 1846$ . To seed the instability, the electrons have a small initial temperature  $\langle (\mathbf{p}_0 - \langle \mathbf{p}_0 \rangle)^2 \rangle = \sigma_p^2$ . In relativistically normalized units, the simulation parameters are: the peak plasma density is  $n_0$  with the corresponding non-relativistic plasma frequency  $\omega_p = \sqrt{4\pi n_0 e^2 / m_e}$ . The initial particle momenta  $p_{x0} = -10$  and  $\sigma_p = 10^{-4}$ . The grid steps were  $h_y = h_z = 1.88 c/\omega_p$  and  $h_x = c\tau = \Delta = 0.63 c/\omega_p$ . In the Yee simulation, we used  $c\tau = 0.9 h_x$ . As a diagnostics for the comparison, we selected the growth of the maximum local field intensity  $I = \mathbf{E}^2 + \mathbf{B}^2$  on the grid. The results are shown in Fig.VI.1

We see that the fluctuating fields in simulations using the Yee scheme grow to an unacceptable level within a few plasma oscillations. The noise in the RIP scheme remains many orders of magnitude lower. The slow growth of the noise fields here has nothing to do with the Cerenkov resonance, but is the unavoidable “numerical heating” always present in PIC codes. To demonstrate this, we do another simulation with a stationary plasma,  $\langle \mathbf{p}_0 \rangle / m_\alpha c = (0, 0, 0)$ , while keeping all other parameters the same. We observe nearly the same rate of noise growth in the stationary plasma as in the streaming case. The higher absolute level of the noise for the streaming plasma is the natural consequence of the larger initial noise current source in this case. Fig.VI.1 demonstrates clearly that the RIP scheme is free from Cerenkov instability for plasmas drifting along the selected axis.

### B. Laser-driven plasma bubble

As the second numerical test, we select laser-plasma particle acceleration in the bubble regime [40]. A circularly polarized laser pulse with initial vector potential  $e\mathbf{A}/mc = \Re[a(\xi, \mathbf{r}_\perp)(\mathbf{e}_y + i\mathbf{e}_z) \exp(ik\xi)]$  is used. Here,  $\xi = x - ct$  and the envelope shape has been selected as a spherical Gaussian  $a(\xi, \mathbf{r}_\perp) = a_0 \exp(-\xi^2/\sigma_\parallel^2 - r_\perp^2/\sigma_\perp^2)$  with the amplitude  $a_0 = 5$ , length  $\sigma_\parallel = 5\lambda$  and radius  $\sigma_\perp = 5\lambda$ , where the laser wavelength  $\lambda = 2\pi/k$ . The plasma consists of electrons and protons. At the plasma boundary, the density increases linearly from  $n = 0$  to  $n = 0.01 n_c$  over a length  $L = 38\lambda$ . Here  $n_c = m_e \omega^2 / 4\pi e^2$  is the critical density. The simulation results after an acceleration distance of  $L_a = 300\lambda$  are shown in Fig.VI.2. The simulation box has a size  $40\lambda \times 40\lambda \times 40\lambda$ . The grid steps are  $h_x = 0.05\lambda$ ,  $h_y = 0.25\lambda$ ,  $h_z = 0.05\lambda$  and the time step is  $\tau = 0.9 h_x/c$  in the Yee simulation, and  $\tau = h_x/c$  in the RIP simulation.

We see that the electron bunch trapped by the bubble has a fine longitudinal structure in the Yee simulation. At the same time, the bubble accelerating field  $E_x$  is modulated by the short-wavelength radiation emitted by the

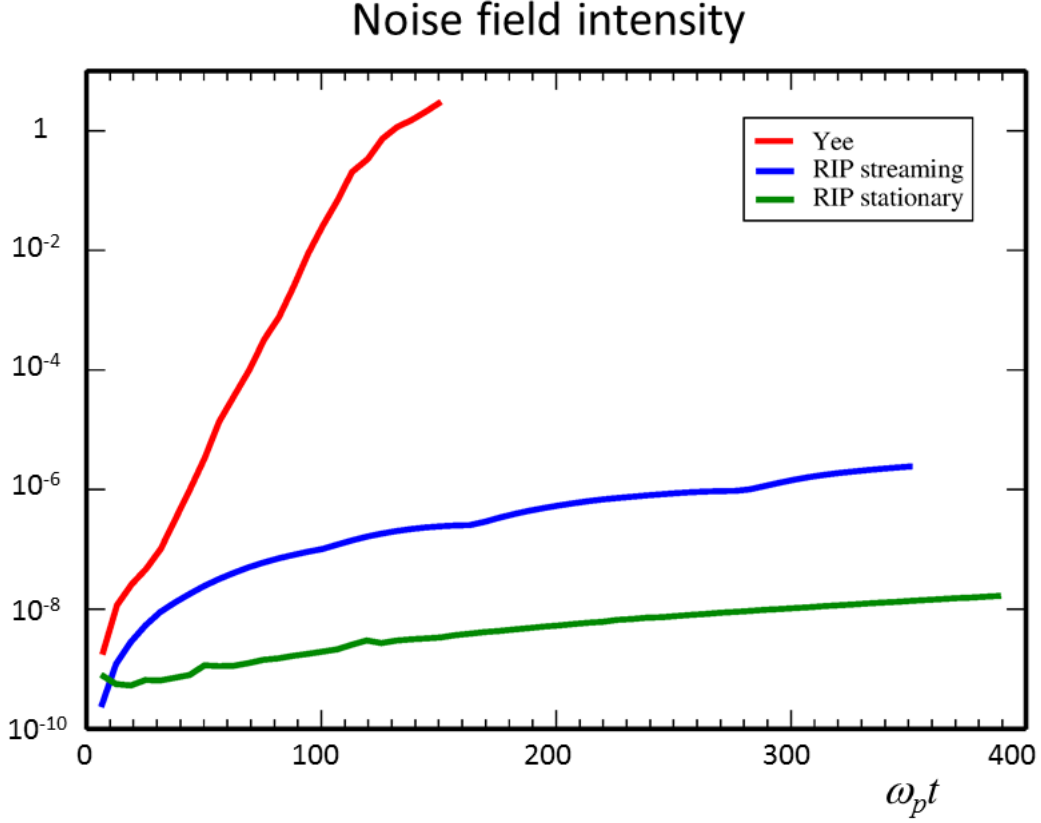


Figure VI.1. Growth of fluctuating fields in the “streaming plasma” simulations. The Yee scheme is fully subject to the numerical Cerenkov instability. The RIP simulation of streaming plasma shows several orders of magnitude lower noise fields. The noise field growth rate is nearly the same as in the stationary case and is due to the standard numerical heating in PIC codes.

relativistic electrons due to the numerical Cerenkov resonance. This numerical emission is clearly seen in Fig. VI.2(c) as the bow-like short wavelength radiation emanating from the dense electron bunch. The RIP simulation shows a rather smooth electron bunch and no signatures of numerical Cerenkov emission. The  $E_z$ -field of the relativistic electron bunch has a clean quasi-static form: it is not bow-shaped, but perpendicular to the bunch. Further, the Yee scheme shows a small additional numerical dephasing can be observed at the leading edge of the bubble. Also of note is the difference in the laser field phase in the Yee case as compared with the RIP simulations, as seen in the longitudinal electric field shown in the middle column in Fig. VI.2 and the electron density distribution in frames Fig. VI.2(a),(e),(h).

To check the RIP scheme convergence, we did an additional simulation with lower resolution. We doubled the longitudinal grid step and the time step to  $h_x = c\tau = 0.1\lambda$ , such that we have only 10 cells per laser wavelength. The results are shown in the last row in Fig. VI.2. One observes little difference from the higher resolution simulation, shown in the middle row in Fig. VI.2. Even the laser phase clearly seen in Fig. VI.2(f) and (i) and its action on the electron density at the bubble front, Fig. VI.2(e) and (h), is the same. This demonstrates excellent convergence properties of the RIP scheme.

### C. Quasi-linear wake

Finally, we check how well the RIP scheme describes the long term evolution of a quasi-linear wake in plasma. We take a spherical Gaussian proton bunch  $n_p = n_0 \exp\left(-\xi^2/\sigma_{||}^2 - r_{\perp}^2/\sigma_{\perp}^2\right)$  with the peak bunch density  $n_p = 0.2n$  and the radii  $\sigma_{||} = \sigma_{\perp} = c/\omega_p$ , where  $\omega_p = \sqrt{4\pi n e^2/m_e}$  is the background plasma frequency. The grid steps are  $h_x = c\tau = 0.125 k_p^{-1}$ ,  $h_y = h_z = 0.2 k_p^{-1}$ , where  $k_p = \omega_p/c$  is the plasma wave number. The background plasma is represented by 8 macroparticles per cell and the proton bunch has a single macroparticle per cell. The protons have

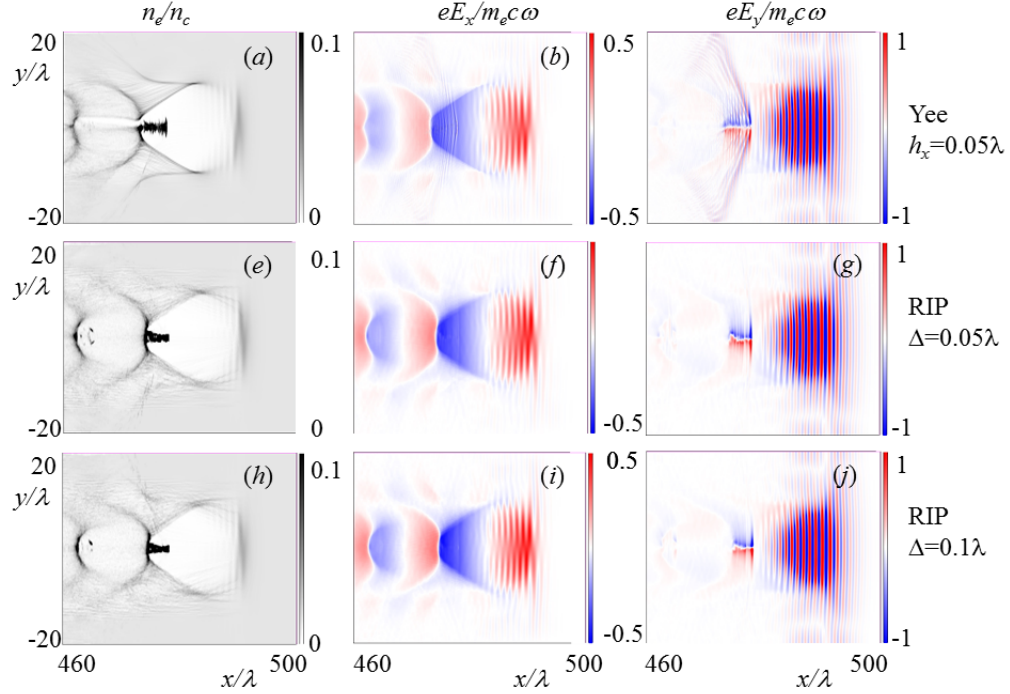


Figure VI.2. Laser-plasma wake field acceleration in the bubble regime. The columns from left to right show electron plasma density  $n_e/n_c$ , the accelerating electric field  $eE_x/mc\omega$  and the transverse electric field  $eE_y/mc\omega$  after the laser pulse propagated  $L_a = 300\lambda$ . The first row shows the Yee scheme simulation results for the longitudinal grid step  $h_x = 0.05\lambda$  and time step  $\tau = 0.04\lambda/c$ , the middle row gives the RIP scheme results with the same grid steps and time step  $c\tau = h_x = 0.05\lambda$ , and the last row shows RIP scheme results with two times rougher resolution in the propagation direction  $h_x = c\tau = 0.1\lambda$ . The numerical Cerenkov resonance in the Yee scheme is clearly seen in frame (c) as the short wavelength bow-like emission by the accelerated electron bunch.

energy of 400 GeV. The resulting wake field is shown in Fig. VI.3.

The electron density perturbation is significant and reaches  $\delta n/n \approx 0.5$ . No numerical Cerenkov emission by the relativistic proton driver is observed. The wake phase front curvature changes sign from negative at the position of the proton bunch driver to positive far behind it. This curvature change is well known and is due to relativistic effects [41]. We see that the RIP scheme is robust and well describes long quasi-linear wakes.

## VII. DISCUSSION

The new RIP scheme is a compact stencil FDTD Maxwell solver that removes numerical dispersion in one selected direction. For the waves propagating in the transverse direction, it corresponds to the Yee solver. The RIP scheme is local and does not use any global spectral methods. This allows for efficient parallelization via domain decomposition in all three dimensions. The computational cost of the RIP solver is comparable with that of the Yee solver. The solver does require a grid uniformly spaced in the propagation direction and the time step must be equal to the grid step  $\tau = h_x/c$ . The discretization in the transverse plane, however, can be arbitrary and even unstructured. The RIP solver is most suitable for simulations of quasi-1D physics problems such as laser wake-field acceleration.

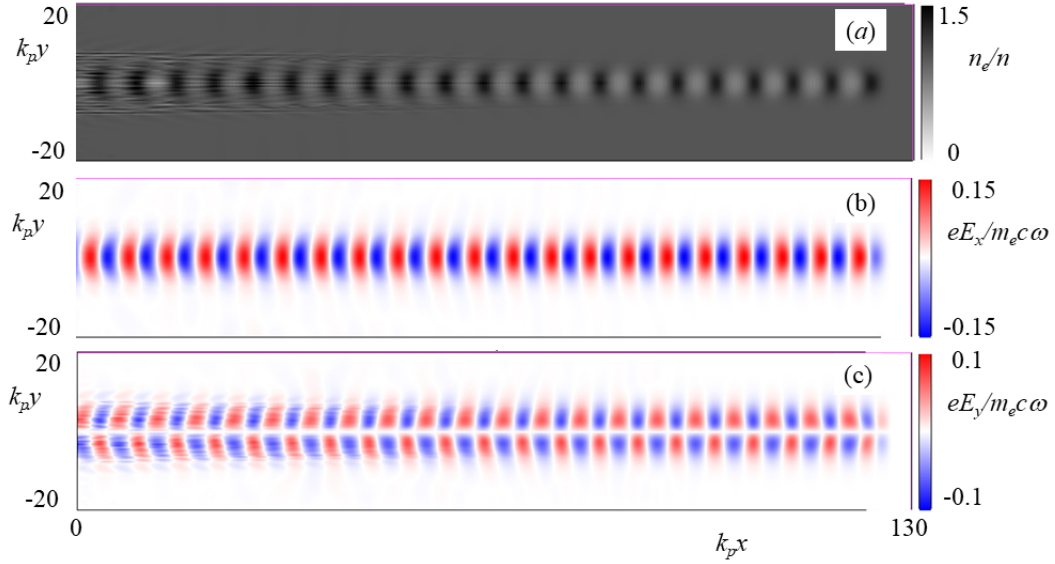


Figure VI.3. Quasilinear wake field generation by a short proton bunch. (a) electron density; (b) longitudinal electric field  $eE_x/mc\omega$ ; (c) transverse electric field  $eE_y/mc\omega$ ;

### ACKNOWLEDGEMENTS

This work has been supported in parts by BMBF and DFG (Germany).

- 
- [1] ALEGRO Collaboration, “Towards an Advanced Linear International Collider” arXiv:1901.10370 (2019)
  - [2] W. Leemans and E. Esarey, “Laser-driven plasma-wave electron accelerators” *Physics Today* **62**, 3, 44 (2009)
  - [3] | <http://eupraxia-project.eu>
  - [4] C. Joshi and A. Caldwell, “Plasma Accelerators”, in *Accelerators and Colliders*, edited by S. Myers and H. Schopper (Springer Berlin Heidelberg, Berlin, Heidelberg, 2013), Chap. 12.1, pp. 592 – 605.
  - [5] T. Tajima and J. M. Dawson. *Phys. Rev. Lett.* **43**, 267 (1979)
  - [6] E. Esarey, C. B. Schroeder, W. P. Leemans, *Rev. Mod. Phys.* **81**, 1229 (2009).
  - [7] Fonseca RA, Martins SF, Silva LO, Tonge JW, Tsung FS, Mori WB, “One-to-one direct modeling of experiments and astrophysical scenarios: pushing the envelope on kinetic plasma simulations”, *Plasma Physics and Controlled Fusion* vol. **50**, 124034 (2008)
  - [8] A. Pukhov, “Particle-In-Cell Codes for Plasma-based Particle Acceleration”, CERN Yellow Rep. 1 , 181 (2016).
  - [9] T.D.Arber, K.Bennett, C.S.Brady, A.Lawrence-Douglas, M.G.Ramsay, N.J.Sircombe, P.Gillies, R.G.Evans, H.Schmitz, A.R.Bell and C.P.Ridgers. “Contemporary particle-in-cell approach to laser-plasma modelling”, *Plasma Phys. Control. Fusion* **57**, 113001 (2015).
  - [10] Jean-Luc Vay, Irving Haber, Brendan B. Godfrey, “A domain decomposition method for pseudo-spectral electromagnetic simulations of plasmas”, *Journal of Computational Physics* **243**, 260 (2013).
  - [11] J. Derouillat, A. Beck, F. Prez, T. Vinci, M. Chieramello, A. Grassi, M. Fl, G. Bouchard, I. Plotnikov, N. Aunai, J. Dargent, C. Riconda, M. Grech, SMILEI: a collaborative, open-source, multi-purpose particle-in-cell code for plasma simulation, *Comput. Phys. Commun.* **222**, 351-373 (2018)
  - [12] C.K. Birdsall and A.B. Langdon, *Plasma Physics via Computer Simulations* (Adam Hilger, New York, 1991). <http://dx.doi.org/10.1887/0750301171>
  - [13] A. J. Gonsalves, K. Nakamura, J. Daniels, C. Benedetti, C. Pieronek, T. C. H. de Raadt, S. Steinke, J. H. Bin, S. S. Bulanov, J. van Tilborg, C. G. R. Geddes, C. B. Schroeder, Cs. Toth, E. Esarey, K. Swanson, L. Fan-Chiang, G. Bagdasarov, N. Bobrova, V. Gasilov, G. Korn, P. Sasorov, and W. P. Leemans “Petawatt Laser Guiding and Electron Beam Acceleration to 8 GeV in a Laser-Heated Capillary Discharge Waveguide” *Phys. Rev. Lett.* **122**, 084801
  - [14] I. Blumenfeld, C. E. Clayton, F.-J. Decker, M. J. Hogan, C. Huang, R. Ischebeck, R. Iverson, C. Joshi, T. Katsouleas, N. Kirby, W. Lu, K. A. Marsh, W. B. Mori, P. Muggli, E. Oz, R. H. Siemann, D. Walz, and M. Zhou, “Energy doubling of 42 GeV electrons in a metre-scale plasma wakefield accelerator” *Nature (London)* **445** , 741 (2007).

- [15] E. Adli et al., AWAKE collaboration “Acceleration of electrons in the plasma wakefield of a proton bunch”, *Nature* **561** (7723), 363 (2018)
- [16] C. Huang, V.K. Decyk, C. Ren, M. Zhou, W. Lu, W.B. Mori, J.H. Cooley, T.M. Antonsen, T. Katsouleas “QUICKPIC: A highly efficient particle-in-cell code for modeling wakefield acceleration in plasmas” *Journal of Computational Physics* **217** (2006) 658–679
- [17] K. V. Lotov, “Fine wakefield structure in the blowout regime of plasma wakefield accelerators” *Phys. Rev. ST Accel. Beams* **6**, 061301 (2003).
- [18] P. Mora and Th. Antonsen Jr “Kinetic modeling of intense, short laser pulses propagating in tenuous plasmas” *Phys. Plasmas*, **4**, 217 (1997).
- [19] J.-L. Vay “Noninvariance of Space- and Time-Scale Ranges under a Lorentz Transformation and the Implications for the Study of Relativistic Interactions” *Phys. Rev. Lett.* **98**, 130405 (2007)
- [20] B. Godfrey, Numerical Cherenkov instabilities in electromagnetic particle codes, *Journal of Computational Physics* **15** (4) (1974) 504–521.
- [21] Yee K S “Numerical solution of initial boundary value problems involving maxwell’s equations in isotropic media” 1966 *IEEE Trans. Antennas Propag.* **14**, 302–7
- [22] J.-L. Vay, C.G.R. Geddes, E. Cormier-Michel, D.P. Grote “Numerical methods for instability mitigation in the modeling of laser wakefield accelerators in a Lorentz-boosted frame” *Journal of Computational Physics* **230** (2011) 5908–5929.
- [23] D.-Y. Na , J. L. Nicolini , R. Lee , B.-H. V. Borges , Y. A. Omelchenko , F. L. Teixeira “Diagnosing numerical Cherenkov instabilities in relativistic plasma simulations based on general meshes” arXiv:1809.05534 (2019)
- [24] J. R. Nutter, V. Tikhonchuk, Suppressing the numerical cherenkov radiation in the yee numerical scheme, *Journal of Computational Physics* **305** (2016) 664 – 676. doi:https://doi.org/10.1016/j.jcp.2015.10.057.
- [25] R. Lehe, A. Lifschitz, C. Thaur, and V. Malka “Numerical growth of emittance in simulations of laser-wakefield acceleration”, *PHYSICAL REVIEW SPECIAL TOPICS - ACCELERATORS AND BEAMS* **16**, 021301 (2013)
- [26] A. Pukhov “Three-dimensional electromagnetic relativistic particle-in-cell code VLPL (Virtual Laser Plasma Lab)”, *J. Plasma Phys.* **61**, 425 (1999)
- [27] Benjamin M. Cowan, David L. Bruhwiler, John R. Cary, and Estelle Cormier-Michel, Cameron G. R. Geddes “Generalized algorithm for control of numerical dispersion in explicit time-domain electromagnetic simulations” *PHYSICAL REVIEW SPECIAL TOPICS - ACCELERATORS AND BEAMS* **16**, 041303 (2013)
- [28] J.B. Cole “High-accuracy Yee algorithm based on nonstandard finite differences: new developments and verifications” *IEEE Transactions on Antennas and Propagation* **50**, 1185 - 1191 (2002)
- [29] I. Haber, R. Lee, H. Klein, J. Boris, Advances in electromagnetic simulation techniques, in: *Proc. Sixth Conf. on Num. Sim. Plasmas*, Berkeley, CA, 1973, pp. 46–48.
- [30] Buneman, O., Barnes, Barnes, C. W., Green, J. C., and Nielsen, D. E., Review: “Principles and capabilities of 3-d, E-M particle simulations”, *J. Comput. Phys.*, **38**, 1, 1980.
- [31] Buneman, O “Multidimensional Particle Codes - Their Capabilities and Limitations” *Space Science Reviews*, **42**, Issue 1-2, pp. 103-112 (1985)
- [32] P. Lee, J.-L. Vay “Convergence in nonlinear laser wakefield accelerators modeling in a Lorentz-boosted frame” *Computer Physics Communications* **238** (2019) 102–110
- [33] H. Vincenti and J.-L. Vay, “Ultrahigh-order Maxwell solver with extreme scalability for electromagnetic PIC simulations of plasmas”, *Computer Physics Communications* **228**, 22-29 (July 2018), <https://doi.org/10.1016/j.cpc.2018.03.018>
- [34] Brendan B. Godfrey “Review and Recent Advances in PIC Modeling of Relativistic Beams and Plasmas” arXiv:1408.1146 (2014)
- [35] C. Canuto, M. Hussaini, A. Quarteroni and T. Zang. *Spectral Methods. Fundamentals in Single Domains*. Springer Verlag, 2006.
- [36] G. S. Patterson and S. A. Orszag, “Spectral calculations of isotropic turbulence: Efficient removal of aliasing interactions,” *Phys. Fluids* **14**, 2538–2541 (1971).
- [37] B.B. Godfrey, J.-L. Vay, *Comput. Phys. Comm.* **196** (2015) 221–225, <http://dx.doi.org/10.1016/j.cpc.2015.06.008>.
- [38] Fei Li, Peicheng Yu, Xinlu Xu, Frederico Fiuza, Viktor K. Decyk, Thamine Dalichaouch, Asher Davidson, Adam Tableman, Weiming An, Frank S. Tsung, Ricardo A. Fonseca, Wei Lu, Warren B. Mori “Controlling the numerical Cerenkov instability in PIC simulations using a customized finite difference Maxwell solver and a local FFT based current correction” *Computer Physics Communications* **214** (2017) 6–17
- [39] J. Villasenor and O. Buneman “Rigorous charge conservation for local electromagnetic field solvers” *Computer Physics Communications* **69**, 306-316 (1992)
- [40] A. Pukhov and J. Meyer-ter-Vehn, “Laser wake field acceleration: the highly non-linear broken-wave regime” *Appl. Phys.* **B74** (2001) 355.
- [41] SV Bulanov, F Pegoraro, AM Pukhov, AS Sakharov “Transverse-wake wave breaking” *Physical review letters* **78**, 4205 (1997)